minerals

MDPI

Article

Genesis of the Xiangshan Uranium Ore Field: Implications from Tescan Integrated Mineral Analyzer and Micro-X-Ray Fluorescence Mapping and Thermodynamic Modeling

Xiang Yu [1,2,3], Xuebin Su [2,3,*], Zhe Wang [1], Zongyu Hou [1], Boping Li [2,4], Teng Deng [5,6,7] and Zhaobin Yan [5,6,7]

1 State Key Laboratory of Power System Operation and Control, Tsinghua-Rio Tinto Joint Research Centre for Resources, Energy and Sustainable Development, International Joint Laboratory on Low Carbon Clean Energy Innovation, Department of Energy and Power Engineering, Institute for Carbon Neutrality, Tsinghua University, Beijing 100084, China; yuxiang219@126.com (X.Y.); 15110104633@139.com (Z.W.); houzy@tsinghua.edu.cn (Z.H.)
2 National Key Laboratory of Uranium Resources Exploration-Mining and Nuclear Remote Sensing, Beijing 100029, China; wwwlbp@126.com
3 China National Uranium Corporation, Beijing 100013, China
4 Beijing Research Institute of Uranium Geology, Beijing 100029, China
5 National Key Laboratory of Uranium Resources Exploration-Mining and Nuclear Remote Sensing, East China University of Technology, Nanchang 330013, China; dengteng2015@126.com (T.D.); 200560025@ecut.edu.cn (Z.Y.)
6 School of Earth Sciences, East China University of Technology, Nanchang 330013, China
7 State Key Laboratory of Nuclear Resources and Environment, East China University of Technology, Nanchang 330013, China
* Correspondence: suxuebin1968@163.com

Abstract: Hydrothermal alteration provides critical information for both the exploration and scientific research of hydrothermal uranium deposits. The Xiangshan uranium ore field, the largest volcanic-hosted uranium deposit in China, is characterized by different alterations, including hematitization, illitization, sericitization, chloritization, carbonation and silicification. However, the mineralogical and geochemical characteristics of hydrothermal alterations and their relationships with uranium mineralization remain unclear. In this study, we conducted detailed petrography, TIMA mapping, μ-XRF analyses, mass balance calculations and thermodynamic modeling on the hematitized and illitized porphyritic lava from the Zoujiashan deposit in the Xiangshan ore field. During hematitization, hematite and albite are produced, while quartz, K-feldspar, chlorite, sericite and biotite are consumed, consistent with the increase in Na_2O, Al_2O_3, Fe_2O_3-T, U, As, Pb, Cu, Sc, V, Zr, Y, Hf and Th and the loss of K_2O, MgO, Li, Zn, Ni and Ba. The production of hydrothermal hematite, illite and sericite indicates that the ore fluids are acidic and oxidized. Such physiochemical conditions are favorable for uranium transport as UO_2Cl_2(aq), UO_2SO_4(aq) and UO_2OH^+. Geological processes such as fluid–rock interactions, fluid mixing and fluid boiling could cause fO_2(g) decrease, pH increase and temperature decrease and therefore result in the decrease in uranium solubility and mineralization.

Keywords: Xiangshan uranium deposit; Xiangshan volcanic basin; hydrothermal alteration; hematitization–illitization; thermodynamic modeling

Academic Editors: Glenn Bark and Alan R. Butcher

Received: 3 December 2024
Revised: 18 December 2024
Accepted: 19 December 2024
Published: 24 December 2024

Citation: Yu, X.; Su, X.; Wang, Z.; Hou, Z.; Li, B.; Deng, T.; Yan, Z. Genesis of the Xiangshan Uranium Ore Field: Implications from Tescan Integrated Mineral Analyzer and Micro-X-Ray Fluorescence Mapping and Thermodynamic Modeling. *Minerals* **2025**, *15*, 5. https://doi.org/10.3390/min15010005

1. Introduction

Uranium is commonly transported in hydrothermal fluids in the form of hexavalent uranyl ions (UO_2^{2+}), which are generally combined with anion ligands such as Cl^-, CO_3^{2-}, OH^-, F^-, SO_4^{2-} and HPO_4^{2-} in fluids [1–5]. Therefore, the destruction of these complexes

can lead to uranium precipitation. Precipitation mechanisms in hydrothermal uranium deposits include fluid boiling [6], fluid–rock interaction [4,5] and fluid mixing [7,8], which are capable of changing the physiochemical properties of fluids and therefore destroying the stability of uranium-bearing complexes [9]. Among them, fluid–rock interaction can generate apatite, fluorite and other minerals, thus greatly reducing the contents of P and F in fluids [4]. In addition, fluid–rock interaction will also increase the pH of fluids, resulting in a significant reduction in the stability of the UO_2-bearing complex [5,10]. This process is usually accompanied with various host rock alterations, such as illitization, hematitization, chloritization, carbonation, sericitization and silicification [9,11,12].

As an important prospecting indicator, hydrothermal alteration is closely related to mineralization and therefore has great significance for uranium exploration [13,14]. Hydrothermal alteration with changes in colors, elements and minerals of host rocks could cause changes in oxygen fugacity, pH and elemental concentrations in fluids and therefore induce uranium precipitation [8]. The Xiangshan volcanic-type uranium deposit in Jiangxi Province occurs in the volcano-intrusive complexes, which is considered to be of hydrothermal origin [15,16]. The Xiangshan uranium ore field is characterized by multi-stage hydrothermal alterations, including illitization, hematitization, albitization, chloritization, carbonation and silicification [17]. Previous studies suggest that illitization and hematitization indicate acidic and oxidized properties of fluids, while albitization and carbonation demonstrate relatively higher pH conditions [9,16]. Bulk geochemical compositions in rocks with different hydrothermal alterations in Xiangshan suggest that fluid–rock interaction is an important mineralization mechanism and that reduced minerals like biotite could be the reducing agent [17], but other ore precipitation processes induced by fluid–rock interactions have not been discussed. Despite these studies on hydrothermal alterations in Xiangshan, mineralogical and micro-scale geochemical studies are still lacking, hindering the interpretation of ore fluid properties and mineralization mechanisms.

For this study, the Zoujiashan deposit of the Xiangshan uranium ore field was chosen as the research object, with the aims to (1) determine the geological and mineralogical characteristics of hydrothermal alterations through a detailed field investigation, petrographic observation and Tescan Integrated Mineral Analyzer (TIMA) mapping; (2) analyze the geochemical characteristics by micro-X-ray fluorescence (μ-XRF), major and trace elemental analyses and mass balance calculation; and (3) evaluate the genetic association between fluid–rock interaction and uranium precipitation through thermodynamic modeling. Combined with previous studies, the results of this study were used to decipher the impact of host rock alteration on uranium mineralization, as well as its significance for the exploration of the Xiangshan uranium ore field and similar hydrothermal uranium deposits elsewhere.

2. Regional and Ore Deposit Geology

The Xiangshan Volcanic Basin is situated in central and southern regions of the Jiangxi Province [18], along the structural junction of the Yangtze and Cathaysia plates (Figure 1). The basin extends approximately 26.5 km in the east–west direction and about 15 km in the north–south direction, covering an area of roughly 309 km^2 [19,20]. This region has experienced numerous structural and mineralization processes that are conducive to the formation of uranium–multi-metal deposits, generating the largest volcanic-type uranium ore in China [19,21].

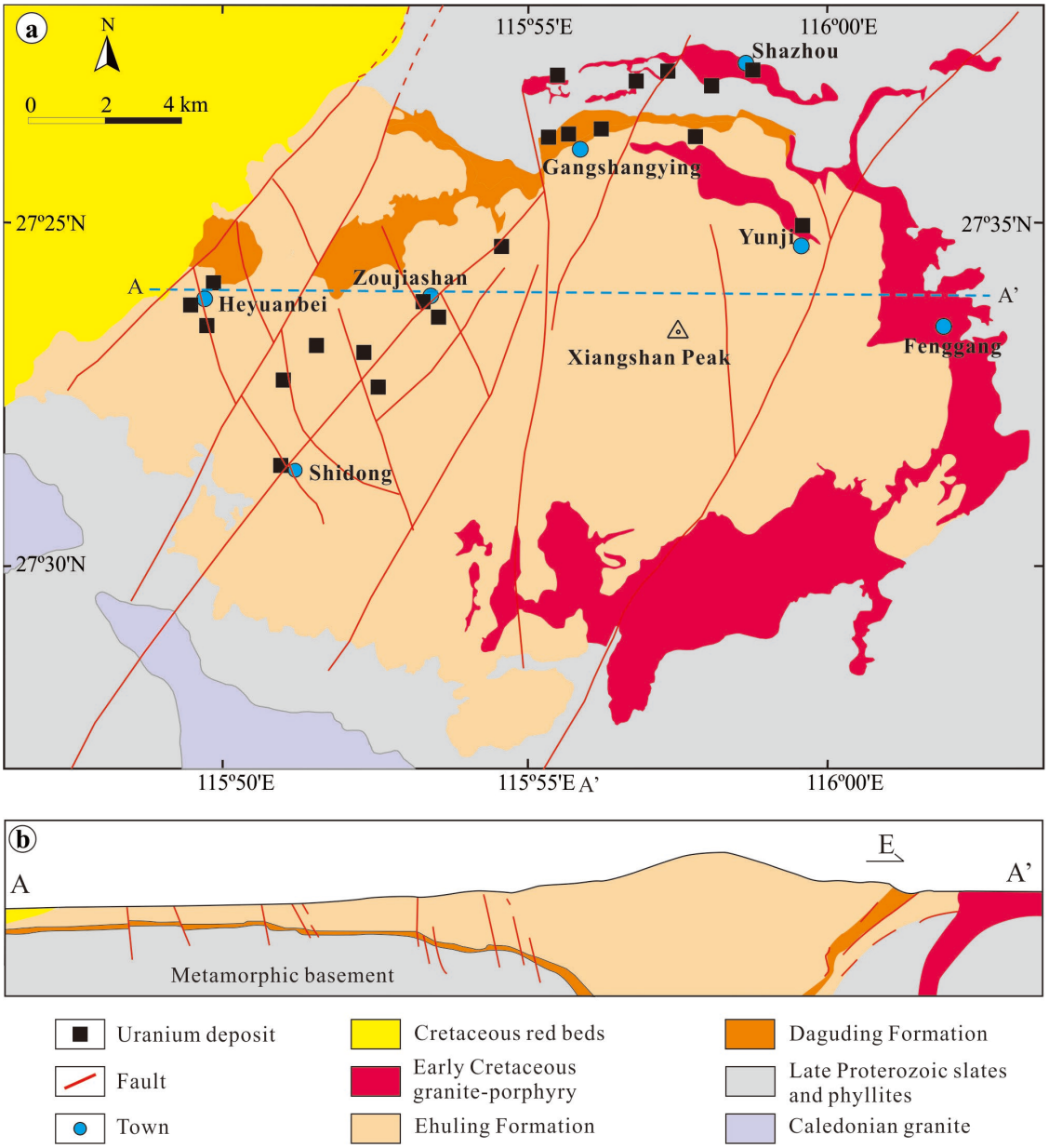

Figure 1. (**a**) Simplified geological map of South China, showing the location of the Gan-Hang belt; (**b**) Geological map of the Xiangshan volcanic basin [16].

The Xiangshan Basin is composed of the basement and cover [22]. The basement consists of Mesoproterozoic schist and amphibole, along with Neoproterozoic phyllite and slate [23]. The rocks in the cover of the basin primarily include two Cretaceous volcanic units, i.e., the lower Daguding and upper Ehuling formations. The Daguding Formation is predominantly composed of purple conglomerates, sandstones and rhyolites, as well as locally occurred volcanic clastic rocks and terrigenous clastic sedimentary rocks [24,25]. The lower layer of the Ehuling Formation mainly comprises volcanic sedimentary sequences, with fragmented lava in the lower part [16,24,26]. Based on the varying lithologies of the Ehuling Formation, it can be further subdivided into three lithofacies from the periphery to center, i.e., the edge, transition and central facies, with fragmented lava being the predominant lithology [26]. The Xiangshan Basin underwent two cycles of volcanic activities [27]. The first cycle was characterized by fissure eruption, while the second cycle featured central eruption [16,28]. In the later stage of volcanic activity, intrusive

rocks are well developed, emplaced in the faults, fractures and extensional structures in an arc-shaped and semi-circular pattern [28].

The structures in the Xiangshan Basin occur in both the basement and cover. The structures in the basement are dominated by EW-trending faults, along with NS-, NE- and NW-trending faults. The cover structures are dominated by NE-trending faults, as well as some EW-, NE- and NW-trending faults [19,29]. The intersection of NE-trending faults, EW-trending faults and volcanic collapse structure controls the localization of uranium deposits [28,30]. The uranium ores in the Xiangshan Basin are mainly concentrated in the northern and western parts of the basin [15,16,27,28].

Many hydrothermal uranium deposits are present in the Xiangshan volcanic basin, and the representative ones are Zoujiashan, Hengjian, Shazhou and Yunji deposits [16,17,30]. The uranium deposits are characterized with different hydrothermal alterations, including hematitization, illitization, albitization, silicification and carbonation [13]. Previous geochronological studies demonstrate that the uranium mineralization in the Xiangshan Basin mainly occurs at ca. 120 Ma and ca. 100 Ma, which is about 15 Ma later than the volcanic rocks but generally consistent with the Cretaceous–Tertiary red beds and mafic rocks [16,31].

The Zoujiashan deposit in the western Xiangshan Basin is the largest uranium deposit in the Xiangshan ore field, with a total uranium reserve of over 10,000 tonnes and average grades ranging from 0.1 to 0.3% [13,30,32,33]. The lithologies in the basement are metamorphic rocks (Figure 2b), primarily comprising biotite quartz schist and sericite schist, locally interspersed with slate and metamorphic sandstone [16,17]. Overlaying the Precambrian basement are Lower Cretaceous volcanic unites, i.e., the Daguding and Eheling formations (Figure 2a,b). The structural layout of the area is predominantly characterized by NE-trending and nearly SN-trending faults (Figure 2a), with the Zou-Shi fault being the most prominent [19,28]. The orebodies are primarily hosted within porphyroclastic lava (Figure 3a), featuring hematite-type and fluorite-type mineralization. The wall rocks in the Zoujiashan deposit are characterized with multiple alterations, such as hematitization, illitization, albitization, chloritization, carbonatization, sericitization and silicification (Figure 3c,d). It is common that fluorite veins are enclosed by hematitized and illitized rocks on both sides (Figure 3c,d). The ore minerals are primarily composed of uraninite, brannerite (Figure 3b), galena, sphalerite, pyrite, hematite, molybdenite, molybdenosulfide, chalcopyrite and minor magnetite [33–35]. The gangue minerals include illite, fluorite, calcite, apatite, quartz, chlorite, K-feldspar and albite, while the common supergene minerals are calcuranite, uranophane and limonite [35].

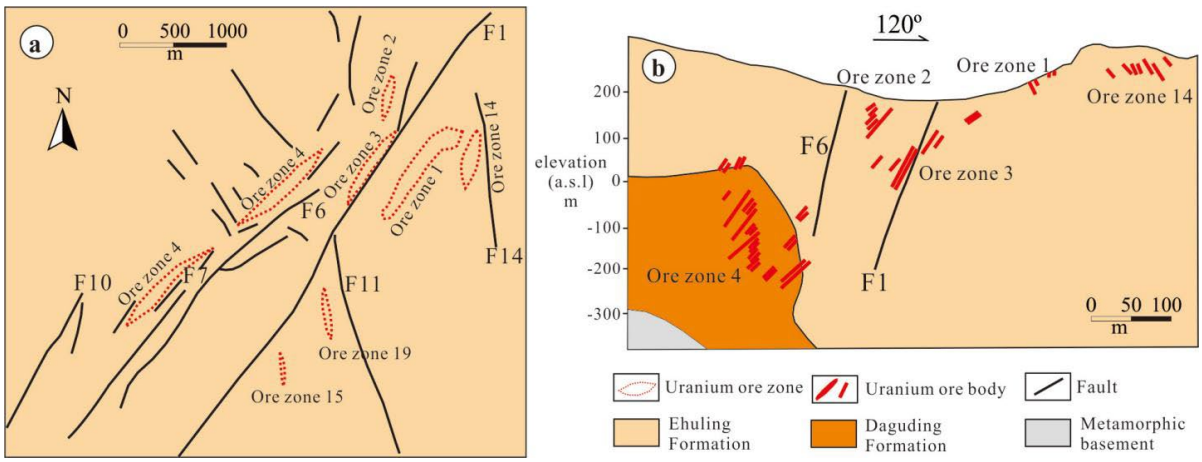

Figure 2. (**a**) Geological map of Zoujiashan deposit; (**b**) Cross-section of Zoujiashan deposit [16].

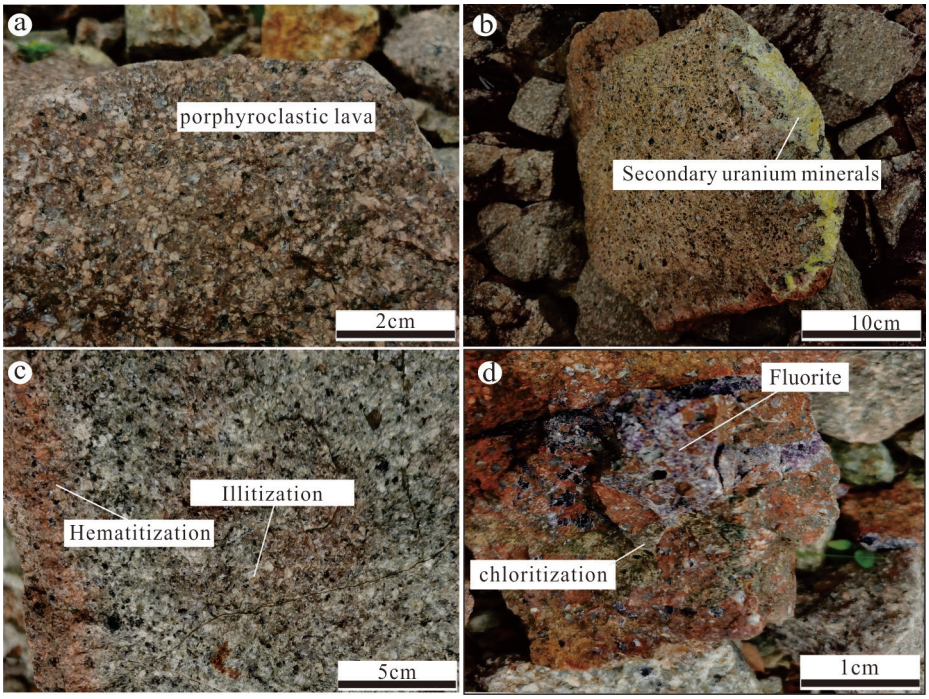

Figure 3. Field petrographic photographs: (**a**) Porphyritic lava sample with (**b**) secondary uranium minerals, (**c**) hematitization and illitization, (**d**) chloritization and fluoritization.

3. Methods

A total of 80 rock samples were collected from the Zoujiashan deposit in this study. Among them, 60 samples were used for preparing thin sections and conducting analyses such as scanning electron microscope (SEM, Zeiss, Bruker, Germany), Tescan Integrated Mineral Analyzer (TIMA, Tescan, Brno, Czech Republic) and microregion X-ray fluorescence surface scan analyses (μ-XRF, Bruker, Karlsruhe, Germany). Thin section observation was conducted on a Leica DM2700P microscope (Leica, Wetzlar, Germany). The remaining samples were used for whole rock major and trace element analyses.

3.1. Tescan Integrated Mineral Analyzer (TIMA)

Mineral composition mapping was conducted on carbon-coated thin sections (mounts) using a MIRA3 scanning electron microscope equipped at Guangzhou Tuoyan Analytical Technology Co., Ltd (Guangzhou, China). We used an acceleration voltage of 25 kV and a probe current of 8.24 nA. The working distance was set at 15 mm. Pixel and dot spacings were set to 3 μm and 9 μm, respectively. The current and BSE signal intensity were adjusted in a platinum Faraday cup using an automated procedure. EDS performance was checked using manganese standards. We used the TIMA liberation analysis module to scan the samples. However, some minerals could not be classified, probably because of (a) the smoothness of the specimen's surface in specific parts, (b) spectral overlaps from small minerals, resulting in multiple superimposed spectra. More than half of the unclassified minerals were less than 3 μm.

3.2. Microarea X-Ray Fluorescence Surface Scan Analysis (μ-XRF)

The μ-XRF surface scan analysis was performed using an M4 Plus Micro Area X-Ray Fluorescence Analyzer at Guangzhou Tuoyan Analytical Technology Co., Ltd. The instrument was equipped with a polycapillary X-ray lens of 20 μm in diameter and two XFlash silicon drift detectors. The scanning was carried out at 50 kV with a current of 600 μA, a step of 20 μm and an acquisition time of 5 ms for a single pixel in 2 mbar air atmosphere.

For different samples, the penetration depth of the X-rays ranges from a few micrometers to hundreds of micrometers. We cleaned the sample surface and removed any loose dust and powder with a rubber bulb or air gun before testing. After testing, we used the M4 Tornado software 1.0 to process the raw data, analyzed the spectral peak information and exported the elemental content information.

3.3. Major and Trace Elemental Analyses and Mass Balance Calculation

Major elements were analyzed by an ED-XRF device at the Laboratory of Analytical Chemistry of the Beijing Research Institute of Uranium Geology (BRIUG) (Beijing, China). The ED-XRF characteristics are listed in Table 1.

Table 1. Characteristics of the ED-XRF system.

	Items	Parameters
X-Ray tube parameters	Voltage/Current	10–50 Kv/0–1 mA
	Collimator diameter	1.0 × 1.0 mm/0.1 × 0.1 mm
	Anode material	Silver
Detector parameters	Detector type	Silicon drift detector (SDD)
	Resolution	@5.9 keV (Fe55) 125–140 eV FWHM
	MAX count rate	2000 k
	Signal-to-noise	15,000:1

During the major element testing, GSR-3, GSD-4, GSD-6, OU-6, GSR-12, GSR-13 and NOD-P-1 were used as standard samples to monitor the accuracy of the results, with the relative standard deviation (RSD) of the test results better than 5%. For the trace element testing, OU-6, BCR-1 and GBPG-1 were used as standard samples to monitor the accuracy of the data, with the RSD of the data better than 5%.

To study the impact of hydrothermal alteration on elemental gain and loss, we adopted the mass balance calculation proposed by Guo et al. [36]. In this research, we applied the isocon diagram method introduced by Grant [37], which is based on the principles established by Gresens [38]. Based on field geological surveys and petrographic observations, P, Ti and Mn were determined to be the immobile elements that best fit the isocon equation. The calculation equation is as follows:

$$\Delta C = \left(C_i^0 / C_i^A\right) \times C^A - C^0$$

In this equation, C^0 and C^A represent the concentrations of each pair of elements in the unaltered and altered samples, respectively. ΔC denotes the gain or loss of major elements per 100 g of rock (in grams) or the parts per million for trace elements. The subscript i indicates the immobile element. ΔC represents the change in element concentration between each pair of samples, where positive values signify an increase in element concentration and negative values signify a decrease.

3.4. Thermodynamic Modeling

Thermodynamic modeling was conducted using the Geochemist's Workbench® (GWB) software package (version 12) [39–41]. Most of the U-bearing minerals and aqueous species were compiled and evaluated by Xing et al. and Deng et al. [9,42], while some are from the Kalintsev et al. and Migdisov et al. [43,44]. All these data were imported into the Unitherm database [45], and the log K values of the associated reactions were calculated and then used to augment the Lawrence Livermore National Laboratory database (the LLNL dataset,

thermo.com.v8.r6+, GWB default database). Activity coefficients were calculated using the B-dot equation [46], and the water dissociation constant was calculated using the equation of Marshall and Franck [47]. The Phase2 program of the GWB software package was used to construct solubility and speciation diagrams.

4. Result

4.1. Petrographic Features

Petrologic observations were conducted on fluorite- and hematite-type ores, as well as illitized porphyritic lava. As shown in Figure 4a, the fluorite grains are generally euhedral and are relatively large, with an average size of >2 mm and featuring growth zones. Hematite grains are locally present within the fluorite veins. Hematite is quite common in hematite-type ores but typically occurs in small sizes (mostly <1 mm). Hematite is present as both fine veinlets and nebulous forms, with the latter being predominant (Figure 4b,c). Biotite has undergone significant metasomatic alteration but retains its original crystallinity, with a size of approximately 1 mm. The altered biotite is complex in compositions, mainly consisting of small (<2 μm) sericite, illite and chlorite. Additionally, pyrite and nebulous hematite can be observed in the surrounding areas (Figure 4c). Albite is also common in illitized rocks, exhibiting characteristic dissolution features of quartz (Figure 4d). Pyrite displays a high degree of automorphic characteristics, with grains approximately 0.2–0.3 mm, while chlorite typically occurs at the boundaries between albite and dissolved quartz grains (Figure 4d). Altered rocks also have hydrothermal K-feldspar, which is relatively fragmented. Uranium minerals are well-developed in pores, with particle sizes of approximately 0.1–0.2 mm, and are spatially associated with fluorite, pyrite, albite and K-feldspar. Notably, pyrite encloses sphalerite, indicating that sphalerite formed prior to pyrite (Figure 4e). Furthermore, we found a large number of altered minerals such as illite, chlorite and muscovite in some samples (Figure 4f).

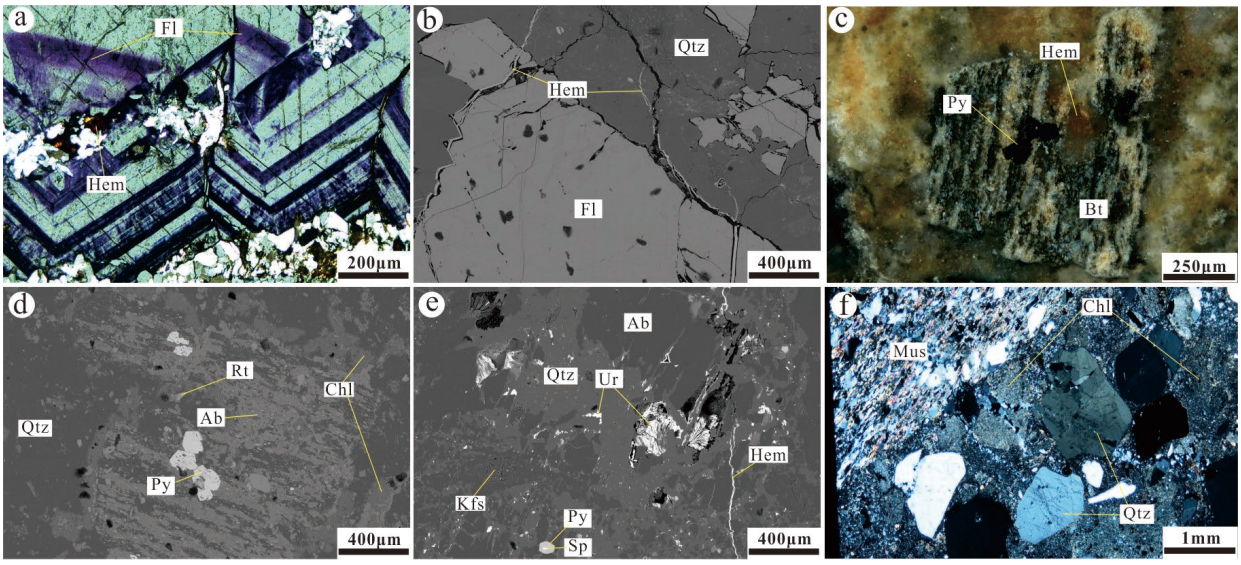

Figure 4. Photographs and photomicrographs of fluorite-type and hematite-type ores, as well as illitized porphyritic lava in the Zoujiashan deposit: (**a**,**b**) Hematite and fluorite; (**c**) Biotite; (**d**) Pyrite and albite; (**e**) Uranium minerals; (**f**) Sericitized sample. Fl, fluorite; Hem, hematite; Qtz, quartz; Py, pyrite; Bt, biotite; Rt, rutile; Ab, albite; Chl, chlorite, Kfs, K-feldspar; Sp, sphalerite; Ur, uraninite; Mus, muscovite.

4.2. Mineral Composition Mapping

The results of TIMA mapping quantitatively indicate the spatial distribution features of modal mineralogy from illitized (Ill) and hematitized (Hem) porphyritic lava (Figure 5a–c). The major minerals of the illitized zone are K-feldspar (41 vol%), quartz (22 vol%), sericite (16 vol%) and albite (10 vol%), with minor chlorite–clinochlore (6 vol%), biotite (3 vol%) and apatite (2 vol%). In the illitized zone, the dissolution of quartz is observed (Figure 5d) and K-feldspar is noticeably albitized (Figure 5e). In addition, chlorite is mainly distributed within K-feldspar grains and the periphery of sericite, and minor apatite is observed in sericite. Locally, biotite is replaced by chlorite and sericite (Figure 5f).

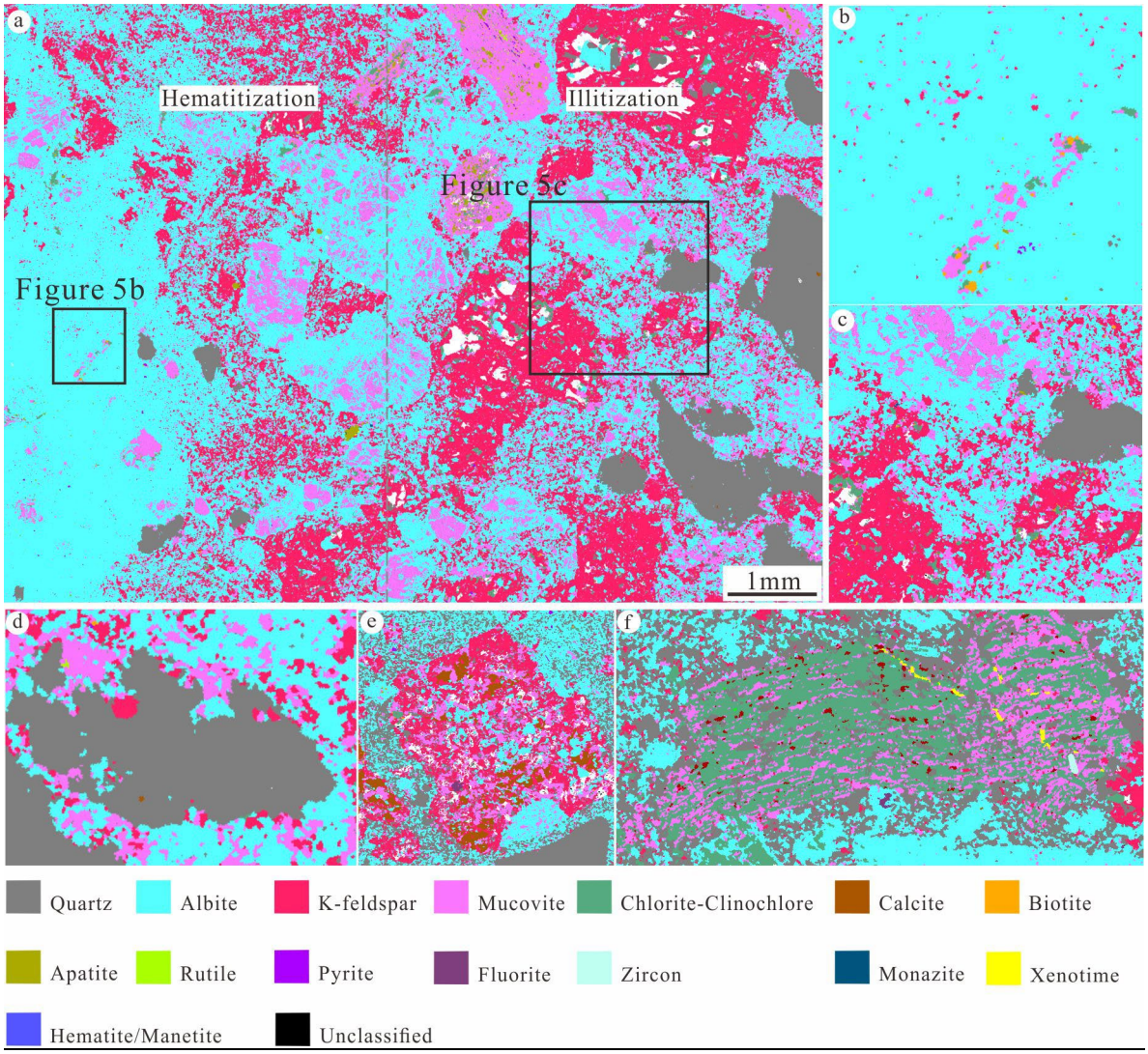

Figure 5. (**a**–**c**): The mineral identification and mapping of hematitized and illitized porphyritic lava by Tescan Integrated Mineral Analyzer (TIMA); (**d**) dissolution of quartz in the illitized zone; (**e**) K-feldspar is albitized; (**f**) biotite is replaced by chlorite and sericite.

The hematitized zone is dominated by albite (91 vol%), with minor K-feldspar (4 vol%), hematite (3 vol%) and sericite (2 vol%). From illitized to hematitized zones, the contents of albite and hematite increase, while the contents of K-feldspar, quartz and sericite decrease. It is noteworthy that K-feldspar, quartz and sericite are uniformly distributed in the altered rocks, and their contents and sizes increase with the distance from the hematitized zone.

4.3. Elemental Mapping

Elemental mapping using μ-XRF on the adjacent illitized and hematitized zones in altered porphyritic lava suggests that most elements have visible zoning (Figure 6). The distribution of Na and K is extremely heterogeneous, and Na is mainly distributed in the hematitized zone (Figure 6a), which is caused by the large amount of albite. However, K is mainly distributed in the illitized zone (Figure 6b), due to the presence of K-feldspar, sericite, chlorite and biotite. The distribution of Fe and Mn is similar. From the illitized to hematitized zones, the contents of Fe and Mn decrease slightly (Figure 6c,d), probably because of the reduction of biotite and chlorite. Additionally, Fe in the hematitized zone is mainly in the form of hematite. Si, Al, Mg and U are relatively evenly distributed in the altered rocks, except that quartz is relatively rich in Si and low in Al content (Figure 6e–h).

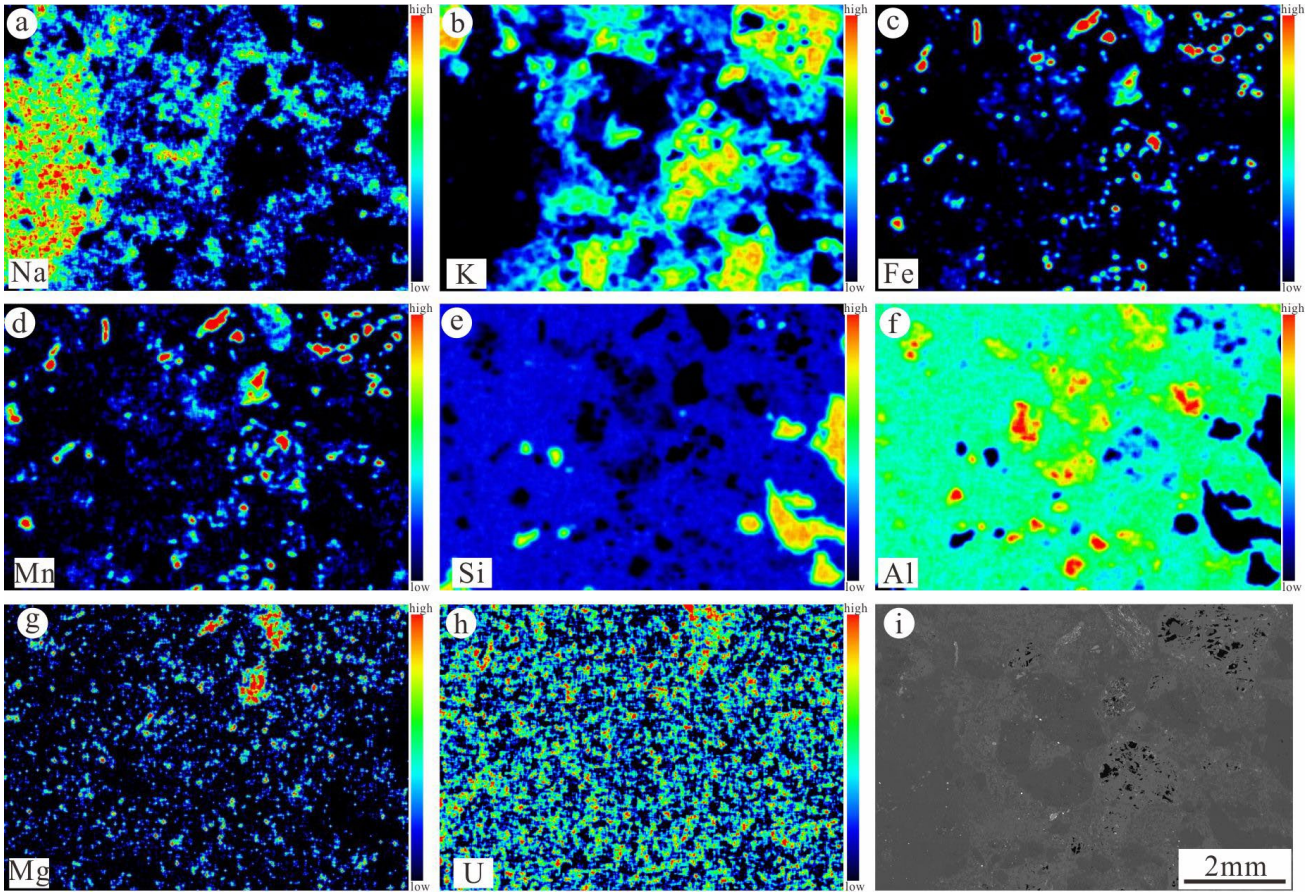

Figure 6. Thin sections of hematitized and illitized porphyritic lava and corresponding micro-X-ray fluorescence (μ-XRF) element mapping of (**a**) Na, (**b**) K, (**c**) Fe, (**d**) Mn, (**e**) Si, (**f**) Al, (**g**) Mg and (**h**) U, illustrating sample-scale chemical characterization. (**i**) Backscattered electron image of hematitized and illitized porphyritic lava.

4.4. Whole-Rock Major and Trace Element Compositions

The major and trace element results for the whole-rock samples are presented in Table 2. In the illitized samples, the ranges of major elements SiO_2, Na_2O, MgO, Al_2O_3, P_2O_5, K_2O, CaO, TiO_2, MnO, Fe_2O_3-T% and LOI are 71.73–77.43 wt%, 2.56–2.75 wt%, 0.17–0.19 wt%, 12.51–15.11 wt%, 0.04–0.07 wt%, 4.19–5.68 wt%, 0.19–1.13 wt%, 0.12 wt%, 0.02–0.04 wt%, 1.05–1.32 wt% and 1.36–1.7 wt%, respectively.

Table 2. Major (%) and trace (ppm) element concentrations of illitized (IS) and hematitized (HS) samples from the Xiangshan deposit.

Sample No.:	XS-S-01IS	XS-S-02IS	XS-S-03IS	XS-S-02-AHS	XS-S-03-BHS	XS-B-02HS	$\Delta C/C^0$
			Major oxides (wt%)				
SiO_2	77.43	71.73	73.81	68.54	69.23	69.10	−0.07
Na_2O	2.56	2.75	2.56	5.47	5.73	6.12	0.52
MgO	0.19	0.18	0.17	0.09	0.11	0.11	−0.70
Al_2O_3	12.51	15.11	14.41	17.72	17.01	17.15	0.18
P_2O_5	0.07	0.04	0.04	0.05	0.05	0.02	−0.24
K_2O	4.19	5.68	5.27	3.80	3.75	2.40	−0.50
CaO	0.19	1.13	0.74	1.33	0.82	1.86	0.46
TiO_2	0.12	0.12	0.12	0.12	0.16	0.11	0.07
MnO	0.02	0.04	0.03	0.03	0.03	0.03	0.00
Fe_2O_3-T	1.05	1.32	1.32	1.52	1.64	1.55	0.21
LOI	1.48	1.70	1.36	1.16	1.29	1.37	−0.18
			Trace elements (ppm)				
Li	48.60	45.90	40.40	21.90	23.30	32.50	−0.70
Be	3.03	3.74	3.30	3.52	3.61	2.40	−0.05
Sc	5.76	7.02	6.48	8.15	8.78	7.60	0.20
V	5.72	6.04	6.11	6.36	8.66	11.40	0.31
Cr	4.06	9.36	6.29	3.08	4.20	3.41	−0.80
Co	0.90	0.99	0.89	0.80	0.59	0.75	−0.28
Ni	2.07	6.43	3.17	2.50	2.36	2.75	−0.51
Cu	3.46	4.70	3.18	4.18	5.93	3.00	0.13
Zn	35.80	27.50	26.10	18.00	22.00	22.90	−0.40
Ga	13.20	15.00	14.70	12.60	13.40	13.30	−0.09
As	5.10	5.08	5.36	41.90	44.40	31.60	0.82
Rb	181.00	183.00	188.00	169.00	157.00	146.00	−0.16
Sr	61.50	81.60	87.60	115.00	110.00	107.00	0.29
Y	29.10	38.20	33.80	46.70	41.60	26.90	0.12
Zr	106.00	108.00	97.20	131.00	143.00	105.00	0.17
Nb	17.10	16.10	16.70	15.40	18.30	13.40	−0.06
Cs	28.20	21.30	20.80	12.50	15.90	17.10	−0.52
Ba	98.90	131.00	121.00	141.00	152.00	46.10	−0.03
La	34.60	32.50	31.10	27.40	30.50	33.00	−0.08
Ce	73.80	69.10	67.00	59.60	65.70	66.40	−0.09
Pr	8.48	7.78	7.64	6.96	7.76	7.32	−0.08
Nd	31.20	29.20	27.40	25.80	28.60	25.60	−0.09
Sm	6.95	6.97	6.45	6.74	7.16	4.93	−0.08
Eu	0.28	0.45	0.42	0.67	0.67	0.17	0.23
Gd	5.84	6.15	5.59	5.98	6.12	4.31	−0.07
Tb	0.91	1.01	0.90	1.09	1.08	0.67	0.01
Dy	5.43	6.60	5.63	7.54	7.33	4.33	0.08
Ho	1.05	1.35	1.14	1.60	1.51	0.92	0.12
Er	2.94	3.78	3.31	4.80	4.44	2.93	0.17
Tm	0.46	0.59	0.52	0.82	0.75	0.50	0.23
Yb	3.04	3.90	3.39	5.54	5.20	3.58	0.26
Lu	0.47	0.63	0.54	0.87	0.82	0.60	0.27
Hf	3.92	4.05	3.71	4.82	4.98	4.02	0.15
Ta	2.08	2.06	2.11	2.00	2.41	2.13	0.04
Pb	27.10	31.00	33.00	54.30	52.60	18.40	0.26
Th	26.70	24.60	23.80	58.80	67.80	25.30	0.48
U	10.20	57.90	45.80	626.00	750.00	647.00	0.90
LREE	155.31	146.00	140.01	127.17	140.39	137.42	−0.09
HREE	49.24	62.21	54.82	74.93	68.85	44.74	0.11
REE	204.55	208.21	194.83	202.10	209.23	182.16	−0.02

The U content ranges from 10.2 to 57.9 ppm. The samples are more enriched in LREEs with contents ranging from 140.01 to 155.31 ppm, while HREE contents are 49.24–62.21 ppm,

and the total REE content is 194.83–208.21 ppm. The large ion lithophile elements (LILEs) such as Rb, Sr, and Ba have concentrations ranging from 181–188 ppm, 61.5–87.6 ppm and 98.9–131 ppm, respectively. High-field-strength elements (HFSEs) such as Nb, Ta, Zr, Hf and Th have concentrations ranging from 16.1–17.1 ppm, 2.06–2.11 ppm, 97.2–108 ppm, 3.71–4.05 ppm and 23.8–26.7 ppm, respectively.

In the hematitized samples, the ranges of major elements SiO_2, Na_2O, MgO, Al_2O_3, P_2O_5, K_2O, CaO, TiO_2, MnO, Fe_2O_3-T% and LOI are 68.54–69.1 wt%, 5.47–6.12 wt%, 0.09–0.11 wt%, 17.01–17.72 wt%, 0.02–0.05 wt%, 2.4–3.8 wt%, 0.82–1.86 wt%, 0.11–0.16 wt%, 0.03 wt%, 1.52–1.64 wt% and 1.16–1.37 wt%, respectively. The U content is higher in these samples compared to the illitized samples, ranging from 626 to 647 ppm. Similar to the illitized samples, the hematitized samples are also more enriched in LREEs and depleted in HREEs, with contents of 127.17–140.39 ppm and 44.74–74.93 ppm, respectively, and a total REE content of 182.16–209.23 ppm. The LILEs such as Rb, Sr and Ba have concentrations ranging from 146–169 ppm, 107–115 ppm and 46.1–152 ppm, respectively. The HFSEs such as Nb, Ta, Zr, Hf and Th have concentrations ranging from 13.4–18.3 ppm, 2–2.41 ppm, 105–143 ppm, 4.02–4.98 ppm and 25.3–67.8 ppm, respectively.

4.5. Mass Balance

In the mass balance calculation, elements P, Mn and Ti, which align on the linear trend line, were selected as reference markers. The fitting curves of these elements were utilized to evaluate elemental gains and losses in the illitized and hematitized samples, as illustrated in Figure 7.

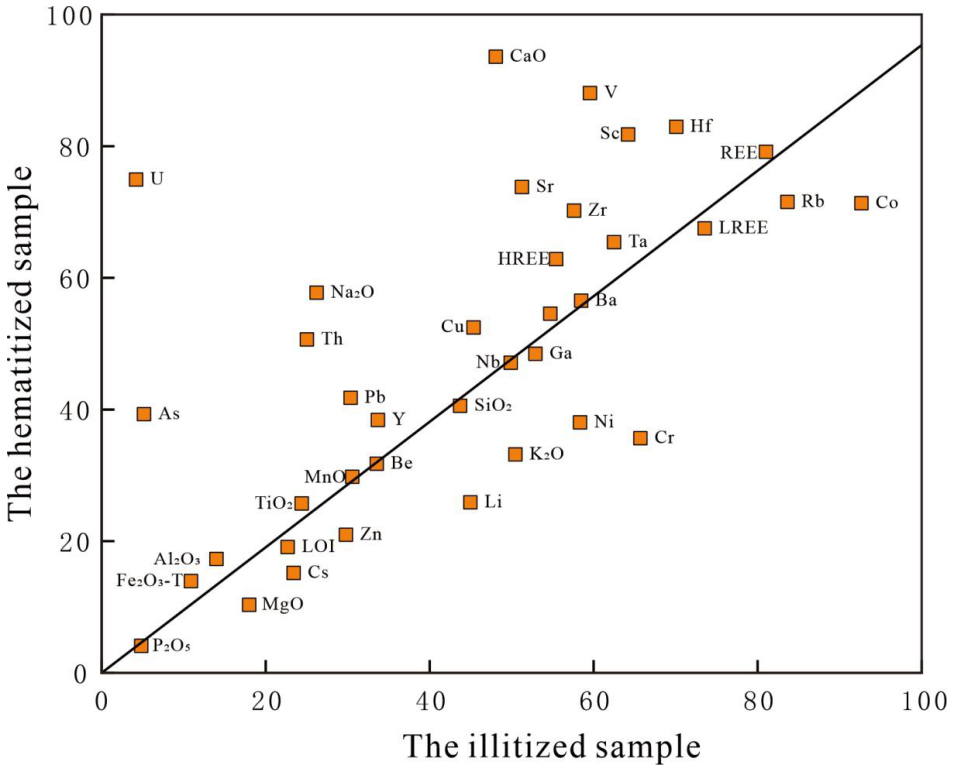

Figure 7. Isocon plots showing the mass transfer between the hematitized and illitized samples.

The results show a significant increase in Na_2O ($\Delta C/C^0 = 0.52$) and Al_2O_3 ($\Delta C/C^0 = 0.18$) contents, likely related to formation of albite during alteration. Notably, Fe_2O_3-T ($\Delta C/C^0 = 0.21$) remains generally constant in both the hematitized and illitized samples, suggesting that Fe in the hematitized rocks is mainly derived from illitized porphyritic lava. Additionally, U ($\Delta C/C^0 = 0.9$) is obviously increased in the hematitized samples, indicating a close association between uranium

mineralization and hematite. Furthermore, the content of CaO ($\Delta C/C^0 = 0.46$) increases due to the formation of carbonate. The hematitization is also marked by an enrichment of chalcophile elements, such as As ($\Delta C/C^0 = 0.82$), Pb ($\Delta C/C^0 = 0.26$) and Cu ($\Delta C/C^0 = 0.13$). Additionally, the decrease in K_2O ($\Delta C/C^0 = -0.5$) and MgO ($\Delta C/C^0 = -0.7$) is associated with the reduction of K-feldspar, sericite, chlorite and biotite. Moreover, Li ($\Delta C/C^0 = -0.7$), Co ($\Delta C/C^0 = -0.28$), Zn ($\Delta C/C^0 = -0.4$), Ni ($\Delta C/C^0 = -0.51$) and Ba ($\Delta C/C^0 = -0.03$) were lost, while Sc ($\Delta C/C^0 = 0.2$), V ($\Delta C/C^0 = 0.31$), Zr ($\Delta C/C^0 = 0.17$), Y ($\Delta C/C^0 = 0.12$), Hf ($\Delta C/C^0 = 0.15$) and Th ($\Delta C/C^0 = 0.48$) were obviously gained.

4.6. Uranium Speciation and Solubility

The fluids used for thermodynamic modeling in this study are characterized by U-Na-Cl-C-P-S-H-O systems. The modeling was performed using the default settings of Geochemist's Workbench, with fluid compositions derived from Deng et al. [9], based on data from Yu et al. [22]. The temperature was set as 250 °C. The solubility and speciation diagrams with log fO_2(g) and pH coordinates are used to figure out the transport and precipitation of uranium in fluids.

As shown in Figure 8, uranium can be dissolved under both oxidized and reduced conditions. Under reduced conditions, uranium in fluids is mainly present as UCl_4(aq). The dissolving of high concentrations of uranium in reduced conditions requires very low pH (pH < 1.8 for 1 ppm U in fluids). In oxidized conditions, uranium can be dissolved in a wider pH range (pH < 5 for 1 ppm U in fluids). The predominant U-bearing aqueous species change with pH. At pH < 2.7, the predominant aqueous species is UO_2Cl_2(aq). At 2.7 < pH < 3.0, UO_2SO_4(aq) is the most important complex. At 3.0 < pH < 4.6, U is mainly present as UO_2OH^+. Under very high pH conditions (>8), U is mainly dissolved as $UO_2(OH)_4^{2-}$. Two U-bearing minerals are present, i.e., the reduced uraninite and oxidized $CaUO_4$.

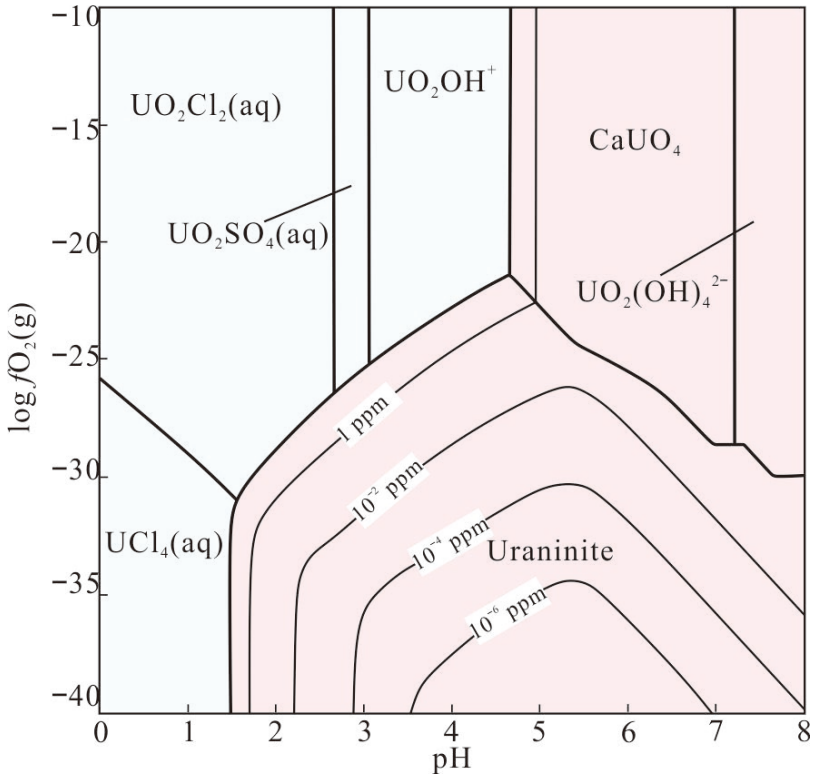

Figure 8. Solubility and speciation diagram of U at 250 °C.

5. Discussion

5.1. Mineralogical and Geochemical Characteristics of Hydrothermal Alteration

This study conducted detailed petrographic and geochemical studies on the adjacent hematitized and illitized porphyritic lava in the Xiangshan uranium ore field. Generally, it is believed that illitization is slightly earlier than hematitization [22,48], therefore comparing the mineralogical and geochemical differences between pre-ore illitization and syn-ore hematitization could provide important insights for uranium mineralization. Compared with illitized rocks, the hematitized rocks have more albite, but less illite, muscovite, chlorite, quartz and K-feldspar (Figures 3 and 4). Hematite is not recognized by TIMA mapping, possibly due to its small sizes (<1 mm, Figure 4). The albite increases and quartz decreases are consistent with quartz dissolution and the presence of albite within the enclaves of quartz grains (Figure 4d). The alteration of K-feldspar leads to the formation of abundant illite and sericite. Biotite is also extensively altered, and many minerals are produced by such fluid–rock interactions, such as chlorite and sericite, as well as a small amount of rutile, uranium minerals and apatite. This is consistent with previous conclusions that biotite is the reducing agent for uranium mineralization [17]. There is also locally occurred syn-ore pyrite in the uranium ores (Figure 4), similar to the discovery in the Yingqian granite-type uranium deposit in the Taoshan-Zhuguang belt [49]. Since it is produced in the syn-ore stage, such pyrite is not the reducing agent for uranium mineralization. Instead, it is likely formed by the continuous decrease in fO_2(g) in fluids during fluid–rock interactions [9]. Consequently, the production of hydrothermal pyrite, common in uranium deposits, does not demonstrate the reducing properties of the initial ore fluids.

The elemental changes during hematitization revealed by μ-XRF and mass balance calculation are closely correlated with mineralogical variation. The increase in U and Th contents demonstrate that the hematitized samples were formed by syn-ore fluids, as evidenced by the production of uranium minerals (Figures 6 and 7). The increase in CaO and Na_2O and decrease in K_2O are related to the production of albite and carbonate, as well as dissolution of K-feldspar, in the altered rocks. The slightly increased Fe contents in the hematitized rocks indicate that aqueous iron from the uraniferous fluids enters the ore during fluid–rock interactions [9]. HREEs are enriched in the uranium ores in the Xiangshan area [49]. The main reason is that heavy rare earth elements can occur in uranium and thorium minerals in the forms of isomorphism and adsorption. In addition, monazite, xenotime and parisite also formed in the uranium ores (Figure 5) [49]. The loss of LREEs is because their leaching rates are higher in acidic environments than those in alkaline conditions. As the uranium ore-forming fluid is acidic, it could cause the loss of LREEs in the host rocks. In addition, the contents of many metal elements, such as Pb, Cu, As and HREEs, increase during alteration, consistent with polymetallic mineralization in the Xiangshan ore field [34,50–52].

5.2. Implications for Uranium Mineralization

Wall-rock alteration with visible color changes and prominent elemental and mineralogical variation is significant for hydrothermal uranium deposits in both exploration and theoretical scientific research [4,10,13,53,54]. Petrographic and geochemical studies, as well as thermodynamic modeling conducted in this work, could be used to analyze the physicochemical conditions of ore fluids. The production of hematite (Figures 3 and 4) indicates that the uraniferous fluids are oxidized, which is consistent with thermodynamic modeling (Figure 8). Even though Timofeev et al. proposed that uranium can be transported as UCl_4 (aq) under reduced conditions [55], thermodynamic modeling demonstrates that it requires very low pH (pH < 1.8 for 1 ppm U in fluids) under the physicochemical conditions in Xiangshan [9,52]. Such fluids would be quite unstable and unlikely to be

transported over long ranges with the pH buffering by minerals in the host rocks, such as felspar, muscovite and biotite. Instead, transport under oxidized conditions as UO_2Cl_2(aq), UO_2SO_4(aq) and UO_2OH^+ is more feasible. Notably, the predominant aqueous species differ slightly from those in Deng et al. [9], due to the newly incorporated thermodynamic database reported by Kalintsev et al. and Migdisov et al. [43,44]. Despite the occurrence of fluorite in veins, F-bearing complexes are not important in the Xiangshan uranium deposit, considering the low fluorite solubility [9]. The locally occurred pyrite co-precipitated with uranium minerals demonstrates that redox reactions occurred during mineralization with the consequential decrease in fO_2(g) in the initial oxidized ore fluids.

The presence of widespread illitization and sericitization demonstrates that ore fluids are initially acidic. This is also consistent with our thermodynamic modeling, as well as previous studies [5,10,54]. As demonstrated by Deng et al. [9], fluids with a pH of 2.8–4.8 could result in the production of sericitization in the Xiangshan ore field. Considering the pH of ~5.5 for neutral fluids at 250 °C [43], fluids with such pH values are slightly acidic and are more capable to transport over long distances. The acidic nature of ore fluids is also favorable for the transport of F in the Ca-bearing fluids of Xiangshan [22]. There are also syn-ore albite and carbonate in the ores, and they are likely produced by pH increase which is also an important trigger for uranium mineralization [10,55]. In addition, pH increase also decreases F solubility and causes the co-precipitation of fluorite with uranium minerals. Consequently, the discrepancy in the interpretation of fluid pH is likely caused by the progressive evolution of fluid properties during fluid–rock interactions.

The above-mentioned fO_2(g) decrease and pH increase could lead to the decrease in uranium solubility in aqueous fluids [8,56,57]. Such changes in physicochemical properties of ore fluids could be caused by many geological processes [3,54]. The decrease in fO_2(g) in ore fluids could be caused by interaction with reduced minerals such as pyrite, biotite and/or graphite in the host rocks [58,59] or mixing with external fluids bearing CH_4, H_2S and CO [6,57,60,61]. In the Xiangshan ore field, biotite in the volcanic-intrusive rocks is an important reducing agent, as evidenced by the occurrence of uranium minerals in the altered biotite (Figure 5f). In addition, pre-ore chlorite may also be a potential reducing agent for uranium precipitation [12]. Such a process would generate hematite-type ores and widespread hydrothermal alteration. Mixing with reducing fluids may also be present based on previous fluid inclusion studies [6,22], which could likely produce the fluorite-type ores. The combination of multiple mineralization mechanisms generates both fluorite- and hematite-type ores.

According to the latest thermodynamic modeling and hydrothermal experiments [62,63], the Fe^{3+} content is very low in weakly acidic medium–low temperature hydrothermal fluids, and Fe^{2+} can be transported in oxidized aqueous fluids. The pH increase caused by fluid–rock interactions could lead to redox reactions between Fe^{2+} and U^{6+} in uraniferous fluids and therefore cause uranium precipitation [9]. Since Fe is slightly gained during hematitization and independent Fe-bearing fluids are absent in the Xiangshan ore field [14,61], it is concluded that aqueous Fe^{2+} in the ore fluids contributes to some of the uranium mineralization [61]. Other mechanisms, such as fluid boiling and temperature drop [17,64], may also be involved in uranium precipitation in Xiangshan.

6. Conclusions

(1) Detailed petrographic observation and TIMA mapping demonstrate that hematite and albite are produced, while quartz, K-feldspar, chlorite, sericite and biotite are consumed during hematitization. The increase in Na_2O, Al_2O_3 and Fe_2O_3-T is caused by the precipitation of hematite and albite. The increase in U, As, Pb, Cu, Sc, V, Zr, Y and Hf is due to the metal elements transferring from the ore-forming fluid into

hematitized rocks. The decrease in K_2O and MgO results from the dissolution of chlorite, biotite and feldspar. In addition, metal elements such as Li, Zn, Ni and Ba are leached from altered rocks into the fluids during hematitization.

(2) The presence of hematite indicates that the ore-forming fluid is oxidized, while the presence of illite and sericite indicates that the ore-forming fluid is acidic. Combined with thermodynamic modeling, it indicates that in a reducing and acidic fluid, uranium is mainly transported in the forms of UO_2Cl_2(aq), UO_2SO_4(aq) and UO_2OH^+.

(3) The fO_2(g) decrease and pH increase caused by fluid–rock interactions or fluid mixing could lead to decreases in uranium solubility and therefore cause metal precipitation. During these geological processes, reducing agents could be the reduced minerals (e.g., biotite, chlorite and pyrite) in the host rocks, reduced gases from external fluids or Fe^{2+} in ore fluids.

Author Contributions: Conceptualization, X.Y. and X.S.; methodology, X.Y.; software, T.D.; validation, Z.W.; formal analysis, Z.H.; investigation, B.L.; resources, X.Y. and Z.Y.; data curation, T.D.; writing—original draft preparation, X.Y.; writing—review and editing, X.S. and T.D; visualization, B.L.; supervision, Z.W. and Z.Y.; project administration, X.S. and B.L.; funding acquisition, B.L. All authors have read and agreed to the published version of the manuscript.

Funding: This work was supported by Uranium Ore Geological Exploration Project of Boping Li (No. D2307).

Data Availability Statement: The data presented in this study are available on request from the corresponding author. The data are not publicly available due to ethical and legal concerns.

Conflicts of Interest: Xiang Yu and Xuebin Su are the employees of China National Uranium Corporation. The paper reflects the views of the scientists and not the company. The authors declare no conflicts of interest.

References

1. Plyasunov, A.V.; Grenthe, I. The temperature dependence of stability constants for the formation of polynuclear cationic complexes. *Geochim. Cosmochim. Acta* **1994**, *58*, 3561–3582. [CrossRef]
2. Shock, E.L.; Sassani, D.C.; Willis, M.; Sverjensky, D.A. Inorganic species in geologic fluids: Correlations among standard molal thermodynamic properties of aqueous ions and hydroxide complexes. *Geochim. Cosmochim. Acta* **1997**, *61*, 907–950. [CrossRef] [PubMed]
3. Guillaumont, R.; Mompean, F.J. *Update on the Chemical Thermodynamics of Uranium, Neptunium, Plutonium, Americium and Technetium*; Errata Update; Elsevier Science: Amsterdam, The Netherlands, 2003; Volume 5, pp. 1–440.
4. Bastrakov, E.N.; Jaireth, S.; Mernagh, T.P. Solubility of uranium in hydrothermal fluids at 25 to 300 C. *Geosci. Aust. Rec.* **2010**, *29*, 1–91.
5. Migdisov, A.A.; Boukhalfa, H.; Timofeev, A.; Runde, W.; Roback, R.; Williams-Jones, A.E. A spectroscopic study of uranyl speciation in chloride-bearing solutions at temperatures up to 250 °C. *Geochim. Cosmochim. Acta* **2018**, *222*, 130–145. [CrossRef]
6. Hu, R.-Z.; Bi, X.-W.; Zhou, M.-F.; Peng, J.-T.; Su, W.-C.; Liu, S.; Qi, H.-W. Uranium Metallogenesis in South China and Its Relationship to Crustal Extension during the Cretaceous to Tertiary. *Econ. Geol.* **2008**, *103*, 583–598. [CrossRef]
7. Fayek, M.; Kyser, T.K.; Burns, P.C.; Finch, R. Stable isotope geochemistry of uranium deposits. *Rev. Mineral.* **1999**, *38*, 181–220.
8. Cuney, M.; Kyser, K. *Geology and Geochemistry of Uranium and Thorium Deposits*; Mineralogical Association of Canada: Québec, QC, Canada, 2015; Volume 46.
9. Deng, T.; Chi, G.; Williams-Jones, A.E.; Li, Z.; Wang, Y.; Xu, D.; Wang, Z. Re-evaluation of equilibrium relationships involving U^{6+}/U^{4+} and Fe^{3+}/Fe^{2+} in hydrothermal fluids and their implications for U mineralization. *Chem. Geol.* **2023**, *625*, 121432. [CrossRef]
10. Richard, A.; Rozsypal, C.; Mercadier, J.; Banks, D.A.; Cuney, M.; Boiron, M.-C.; Cathelineau, M. Giant uranium deposits formed from exceptionally uranium-rich acidic brines. *Nat. Geosci.* **2012**, *5*, 142–146. [CrossRef]
11. Zhang, L.; Chen, Z.; Wang, F.; Zhou, T. Whole-rock and biotite geochemistry of granites from the Miao'ershan batholith, South China: Implications for the sources of granite-hosted uranium ores. *Ore Geol. Rev.* **2021**, *129*, 103930. [CrossRef]

12. Cui, J.-Q.; Yang, S.-Y.; Jiang, S.-Y.; Wang, H.; Zhang, R.-X.; Tang, X.-S.; Yan, Y.-J. The role of uranyl complex decomposition and redox conditions in the precipitation of hydrothermal uranium deposits: Insights from chlorite mineralogy and geochemistry in the Shazhou uranium deposit, Xiangshan, SE China. *Bulletin* **2024**, *136*, 388–402. [CrossRef]
13. Bonnetti, C.; Liu, X.; Cuney, M.; Mercadier, J.; Riegler, T.; Yu, C. Evolution of the uranium mineralisation in the Zoujiashan deposit, Xiangshan ore field: Implications for the genesis of volcanic-related hydrothermal U deposits in South China. *Ore Geol. Rev.* **2020**, *122*, 103514. [CrossRef]
14. Chi, G.; Ashton, K.; Deng, T.; Xu, D.; Li, Z.; Song, H.; Liang, R.; Kennicott, J. Comparison of granite-related uranium deposits in the Beaverlodge district (Canada) and South China—A common control of mineralization by coupled shallow and deep-seated geologic processes in an extensional setting. *Ore Geol. Rev.* **2020**, *117*, 103319. [CrossRef]
15. Chen, Z.L.; Yang, N.; Wang, P.A.; Gong, H.L.; Han, F.B.; Zhou, Y.G.; Shao, F.; Tang, X.; Xu, J.S.; Yu, J.F. Analysis of the tectonic stress field in the Xiangshan uranium ore field, Linchuan area, Jiangxi, China. *Geol. Bull. China* **2011**, *30*, 514–531.
16. Guo, F.; Li, Z.; Deng, T.; Qu, M.; Zhou, W.; Huang, Q.; Shang, P.; Zhang, C.; Yan, Z. Key factors controlling volcanic-related uranium mineralization in the Xiangshan Basin, Jiangxi Province, South China: A review. *Ore Geol. Rev.* **2020**, *122*, 103517. [CrossRef]
17. Deng, T.; Chi, G.; Zhang, X.; Li, Z.; Xu, D.; Li, S.; Du, P.; Shang, P.; Zou, S.; Zhou, W.; et al. Mass Transfer during Hematitization and Implications for Uranium Mineralization in the Zoujiashan Deposit, Xiangshan Volcanic Basin. *J. Earth Sci.* **2022**, *33*, 422–434. [CrossRef]
18. Wei, W.-F.; Chen, X.; Yu, Z.-Q.; Chen, W.-F.; Fang, Q.-C.; Tang, X.-S.; Ling, H.-F. Different hydrothermal fluids inducing alteration and uranium mineralisation in the Baquan deposit of the Xiangshan uranium ore field: Constraints from geochemistry of altered rocks and ores. *Ore Geol. Rev.* **2021**, *139*, 104475. [CrossRef]
19. Guo, F.-S.; Lin, Z.-Y.; Li, G.-R.; Deng, J.-Z.; Xie, C.-F.; Yang, H.-Y.; Wu, Z.-C.; Zhou, W.-P.; Jiang, Y.-B.; Li, H.-X. Study on the geological structure of Xiangshan uranium-bearing volcanic basin: Evidences from magnetotelluric sounding and GOCAD modeling. *Chin. J. Geophys.* **2017**, *60*, 1491–1510.
20. Wang, Y.; Fan, H.; Qin, K.; Evans, N.J.; Zhang, C.; Zou, X.; Pang, Y.; Zhang, H. Mineralization age of the Xiangshan uranium ore field, South China redefined by hydrothermal apatite U-Pb geochronology. *Ore Geol. Rev.* **2023**, *160*, 105586. [CrossRef]
21. Yu, Z.; Liu, L.; Ling, H.; Chen, P.; Xu, G.; Chen, W.; Hu, T.; Huang, D. Apatite as a Probe into the Nature and Origin of Hydrothermal Fluids Responsible for U Leaching in the Lujing Granite-Related U Deposits, South China. *Econ. Geol.* **2023**, *118*, 1177–1199. [CrossRef]
22. Yu, Z.-Q.; Ling, H.-F.; Mavrogenes, J.; Chen, P.-R.; Chen, W.-F.; Fang, Q.-C. Metallogeny of the Zoujiashan uranium deposit in the Mesozoic Xiangshan volcanic-intrusive complex, southeast China: Insights from chemical compositions of hydrothermal apatite and metal elements of individual fluid inclusions. *Ore Geol. Rev.* **2019**, *113*, 103085. [CrossRef]
23. Jiang, Y.-h.; Ling, H.-f.; Jiang, S.-y.; Shen, W.-z.; Fan, H.-h.; Ni, P. Trace element and Sr-Nd isotope geochemistry of fluorite from the Xiangshan uranium deposit, Southeast China. *Econ. Geol.* **2006**, *101*, 1613–1622. [CrossRef]
24. Peng, Z.Y.; Chen, W.F.; Mao, Y.F.; Fang, Q.C.; Tang, X.S.; Ling, H.F. Multiple episodes of the Yanshanian magmatism in Xiangshan uranium ore-field, Jiangxi. *Geol. Rev.* **2018**, *64*, 1413–1437.
25. Yang, Q.K.; Huang, Q.T.; Sun, Q.Z. Geological characteristics of sulfur and lead isotopes in the Xiangshan ore field. *Bull. Mineral. Petrol. Geochem.* **2015**, *34*, 756–762.
26. Wu, Y.-F.; Evans, K.; Fisher, L.A.; Zhou, M.-F.; Hu, S.-Y.; Fougerouse, D.; Large, R.R.; Li, J.-W. Distribution of trace elements between carbonaceous matter and sulfides in a sediment-hosted orogenic gold system. *Geochim. Cosmochim. Acta* **2020**, *276*, 345–362. [CrossRef]
27. Yang, S.; Jiang, S.; Jiang, Y.; Zhao, K.; Fan, H. Zircon U-Pb geochronology, Hf isotopic composition and geological implications of the rhyodacite and rhyodacitic porphyry in the Xiangshan uranium ore field, Jiangxi Province, China. *Sci. China Earth Sci.* **2010**, *53*, 1411–1426. [CrossRef]
28. Chen, Z.L.; Wang, P.A.; Wang, Y.; Shao, F.; Tang, X.; Xu, J.; Yu, J.; Han, F.; Sun, Y. Ore-controlling tectonic analysis and ore-prospecting in Shannan mining area of Xiangshan uranium ore-field, Jiangxi. *J. Earth Sci. Environ.* **2013**, *35*, 8–18.
29. Wang, Y.; Fan, W.; Zhang, G.; Zhang, Y. Phanerozoic tectonics of the South China Block: Key observations and controversies. *Gondwana Res.* **2013**, *23*, 1273–1305. [CrossRef]
30. Fusheng, G.; Haiyan, Y.; Zengqian, H.; Zhichun, W.; Ziyu, L.; Guocan, W.; Linfu, X.; Wanpeng, Z. Structural setting of the Zoujiashan-Julong'an region, Xiangshan volcanic basin, China, interpreted from modern CSAMT data. *Ore Geol. Rev.* **2022**, *150*, 105180. [CrossRef]
31. Fusheng, G.; Haiyan, Y.; Zengqian, H.; Zhichun, W.; Ziyu, L.; Guocan, W.; Linfu, X.; Ye, G.; Wanpeng, Z. Mo deposits in Northwest China: Geology, geochemistry, geochronology and tectonic setting. *Ore Geol. Rev.* **2017**, *81*, 641–671.
32. Dahlkamp, F.J. China, Peoples Republic of. In *Uranium Deposits of the World*; Springer: Berlin/Heidelberg, Germany, 2009.
33. Wang, C.; Li, X.; Wei, X. Apatite at Niutoushan U–PB–ZN deposit in Xiangshan ore field: A tracer for hydrothermal fluid. *Geol. J.* **2021**, *56*, 152–169. [CrossRef]

34. Wang, J.; Nie, J.T.; Guo, J.; Huang, Z.Z.; Li, X.Z. Characteristics of deep polymetallic mineralization in the Xiangshan uranium ore field of Jiangxi Province. *Geol. Explor.* **2016**, *52*, 47–59.
35. Jinrong, L.I.N.; Zhihua, H.U.; Yongjian, W.; Song, Z.; Yi, T. Oreforming age and thermal history of uraniumpolymetallic mineralization in Xiangshan uranium orefield. *Acta Petrol. Sin.* **2019**, *35*, 2801–2816. [CrossRef]
36. Guo, S.; Ye, K.; Chen, Y.; Liu, J.-B. A normalization solution to mass transfer illustration of multiple progressively altered samples using the isocon diagram. *Econ. Geol.* **2009**, *104*, 881–886. [CrossRef]
37. Grant, J.A. The isocon diagram; a simple solution to Gresens' equation for metasomatic alteration. *Econ. Geol.* **1986**, *81*, 1976–1982. [CrossRef]
38. Gresens, R.L. Composition-volume relationships of metasomatism. *Chem. Geol.* **1967**, *2*, 47–65. [CrossRef]
39. Bethke, C.M. *Geochemical and Biogeochemical Reaction Modeling*; Cambridge University Press: Cambridge, UK, 2007; 842p.
40. Bethke, C.M.; Farrell, B.; Yeakel, S. *The Geochemist's Workbench Release 12, GWB Essentials Guide*; Aqueous Solutions. LLC: Champaign, IL, USA, 2018.
41. Bethke, C.M. *Geochemical and Biogeochemical Reaction Modeling*, 3rd ed.; Cambridge University Press: Cambridge, UK, 2022; 495p.
42. Xing, Y.; Mei, Y.; Etschmann, B.; Liu, W.; Brugger, J. Uranium Transport in F-Cl-Bearing Fluids and Hydrothermal Upgrading of U-Cu Ores in IOCG Deposits. *Geofluids* **2018**, *2018*, 1–22. [CrossRef]
43. Kalintsev, A.; Migdisov, A.; Brugger, J.; Xu, H. Uranium (VI) hydrolysis up to 250 °C and its geological implications. *Geochim. Cosmochim. Acta* **2024**, *377*, 68–83. [CrossRef]
44. Migdisov, A.; Bastrakov, E.; Alcorn, C.; Reece, M.; Boukhalfa, H.; Capporuscio, F.A.; Jove-Colon, C. A spectroscopic study of the stability of uranyl-carbonate complexes at 25–150 °C and re-visiting the data available for uranyl-chloride, uranyl-sulfate, and uranyl-hydroxide species. *Geochim. Cosmochim. Acta* **2024**, *in press*. [CrossRef]
45. Shvarov, Y.V.; Bastrakov, E.N. HCh: A software package for geochemical equilibrium modelling. User's Guide. *Aust. Geol. Surv. Organ. Rec.* **1999**, *25*, 61.
46. Helgeson, H.C.; Garrels, R.M.; MacKenzie, F.T. Evaluation of irreversible reactions in geochemical processes involving minerals and aqueous solutions—II. Applications. *Geochim. Cosmochim. Acta* **1969**, *33*, 455–481. [CrossRef]
47. Marshall, W.L.; Franck, E.U. Ion product of water substance, 0–1000 C, 1–10,000 bars New International Formulation and its background. *J. Phys. Chem. Ref. Data* **1981**, *10*, 295–304. [CrossRef]
48. Zhang, C.; Cai, Y.-Q.; Dong, Q.; Xu, H. Cretaceous–Neogene basin control on the formation of uranium deposits in South China: Evidence from geology, mineralization ages, and H–O isotopes. *Int. Geol. Rev.* **2020**, *62*, 263–310. [CrossRef]
49. Wang, Y. Study of Occurrence Characteristics and Enrichment Mechanism of HREE in Zoujiashan Uranium Deposit, Jiangxi Province. Master's Thesis, Chengdu University of Technology, Chengdu, China, 2018. (In Chinese)
50. Liu, J.G.; Li, Z.Y.; Nie, J.T.; Wang, J.; Li, X.Z. Ore fabric and mineralogy of polymetallic mineralization in western Xiangshan uranium orefield, Jiangxi Province. *Miner. Depos.* **2019**, *38*, 367–381.
51. Guo, J.; Li, Z.; Nie, J.; Huang, Z.; Wang, J.; Lai, C.-K. Genesis of Pb–Zn mineralization beneath the Xiangshan uranium orefield, South China: Constraints from H–O–S–Pb isotopes and Rb–Sr dating. *Resour. Geol.* **2018**, *68*, 275–286. [CrossRef]
52. Wei, W.-F.; Liu, B.; Sun, L.-Q.; Wei, G.-Y.; Chen, W.-F.; Chen, X.; Fang, Q.-C.; Tang, X.-S.; Li, J.; Ling, H.-F. Molybdenum isotope variation mechanism and ore-genesis of Niutoushan Pb–Zn sulfide orebodies in the Xiangshan volcanic basin, South China. *J. Geochem. Explor.* **2022**, *242*, 107057. [CrossRef]
53. Kotzer, T.G.; Kyser, T.K. Petrogenesis of the Proterozoic Athabasca Basin, northern Saskatchewan, Canada, and its relation to diagenesis, hydrothermal uranium mineralization and paleohydrogeology. *Chem. Geol.* **1995**, *120*, 45–89. [CrossRef]
54. Cuney, M. The extreme diversity of uranium deposits. *Min. Depos.* **2009**, *44*, 3–9. [CrossRef]
55. Timofeev, A.; Migdisov, A.A.; Williams-Jones, A.E.; Roback, R.; Nelson, A.T.; Xu, H. Uranium transport in acidic brines under reducing conditions. *Nat. Commun.* **2018**, *9*, 1469. [CrossRef]
56. Romberger, S.B. Transport and deposition of uranium in hydrothermal systems at temperatures up to 300 °C: Geological implications. In *Uranium Geochemistry, Mineralogy, Geology, Exploration and Resources*; De Vivo, B., Ippolito, F., Capaldi, G., Simpson, P.R., Eds.; Springer: Dordrecht, The Netherlands, 1984; pp. 12–17.
57. Dargent, M.; Truche, L.; Dubessy, J.; Bessaque, G.; Marmier, H. Reduction kinetics of aqueous U (VI) in acidic chloride brines to uraninite by methane, hydrogen or C-graphite under hydrothermal conditions: Implications for the genesis of unconformity-related uranium ore deposits. *Geochim. Cosmochim. Acta* **2015**, *167*, 11–26. [CrossRef]
58. Ng, R.; Alexandre, P.; Kyser, K.; Cloutier, J.; Abdu, Y.A.; Hawthorne, F.C. Oxidation state of iron in alteration minerals associated with sandstone-hosted unconformity-related uranium deposits and apparently barren alteration systems in the Athabasca Basin, Canada: Implications for exploration. *J. Geochem. Explor.* **2013**, *130*, 22–43. [CrossRef]
59. Ng, R.; Alexandre, P.; Kyser, K. Mineralogical and geochemical evolution of the unconformity-related McArthur River Zone 4 orebody in the Athabasca Basin, Canada: Implications of a silicified zone. *Econ. Geol.* **2013**, *108*, 1657–1689. [CrossRef]

60. Goswami, S.; Upadhyay, P.K.; Saravanan, B.; Natarajan, V.; Verma, M.B. Two types of uranium mineralization in Gulcheru quartzite: Fracture-controlled in Ambakapalle area and litho-controlled in Tummalapalle area, Cuddapah Basin, Andhra Pradesh, India. *China Geol.* **2019**, *2*, 142–156. [CrossRef]
61. Song, H.; Chi, G.; Wang, K.; Li, Z.; Bethune, K.M.; Potter, E.G.; Liu, Y. The role of graphite in the formation of unconformity-related uranium deposits of the Athabasca Basin, Canada: A case study of Raman spectroscopy of graphite from the world-class Phoenix uranium deposit. *Am. Mineral.* **2022**, *107*, 2128–2142. [CrossRef]
62. Scholten, L.; Schmidt, C.; Lecumberri-Sanchez, P.; Newville, M.; Lanzirotti, A.; Sirbescu, M.-L.C.; Steele-MacInnis, M. Solubility and speciation of iron in hydrothermal fluids. *Geochim. Cosmochim. Acta* **2019**, *252*, 126–143. [CrossRef]
63. Gammons, C.H.; Allin, N.C. Stability of aqueous Fe (III) chloride complexes and the solubility of hematite between 150 and 300 °C. *Geochim. Cosmochim. Acta* **2022**, *330*, 148–164. [CrossRef]
64. Dahlkamp, F.J. *Uranium Ore Deposits*; Springer Science & Business Media: Berlin/Heidelberg, Germany, 2013.